

Topological defects in rotating spin-orbit-coupled dipolar spin-1 Bose-Einstein condensates

Ning Su,¹ Qingbo Wang,^{1,2} Jinguo Hu,¹ Xianghua Su,¹ and Linghua Wen^{1,*}

¹Key Laboratory for Microstructural Material Physics of Hebei Province,
School of Science, Yanshan University, Qinhuangdao 066004, China

²School of Physics and Technology, Tangshan Normal University, Tangshan 063000, China

(Dated: October 27, 2020)

We consider the topological defects and spin structures of spin-1 Bose-Einstein condensates (BECs) with spin-orbit coupling (SOC) and dipole-dipole interaction (DDI) in a rotating harmonic plus quartic trap. The combined effects of SOC, DDI and rotation on the ground-state phases of the system are analyzed. Our results show that for fixed rotation frequency structural phase transitions can be achieved by adjusting the magnitudes of the SOC and DDI. A ground-state phase diagram is given as a function of the SOC and DDI strengths. It is shown that the system exhibits rich quantum phases including vortex string phase with isolated density peaks (DPs), triangular (square) vortex lattice phase with DPs, checkerboard phase, and stripe phase with hidden vortices and antivortices. For given SOC and DDI strengths, the system can display pentagonal vortex lattice with DPs, vortex necklace with DPs, and exotic topological structure composed of multi-layer visible vortex necklaces, a hidden giant vortex and hidden vortex necklaces, depending on the rotation frequency. In addition, the system sustains fascinating novel spin textures and skyrmion excitations, such as an antiskyrmion pair, antiskyrmion-half-antiskyrmion (antiskyrmion-antimeron) cluster, skyrmion-antiskyrmion lattice, skyrmion-antiskyrmion cluster, skyrmion-antiskyrmion-meron-antimeron lattice, double-layer half-antiskyrmion necklaces, and composite giant-antiskyrmion-antimeron necklaces.

PACS numbers: 67.85.-d, 03.75.Kk, 03.75.Lm, 03.75.Mn

I. INTRODUCTION

Spin-orbit coupling (SOC) of a quantum particle has a significant influence on many physical phenomena, such as quantum spin Hall effect, topological insulators, and topological superconductors [1, 2]. Recently, the experimental realization of artificial SOC in both Bose-Einstein condensates (BECs) and quantum degenerate Fermi gases provides us an ideal platform to study exotic quantum phenomena and novel states of matter [3–7]. So far, a lot of experimental and theoretical studies of spin-orbit-coupled Bose gases have been focused on the quantum phases of pseudo-spin-1/2 BECs with SOC [8–18]. Particularly, the interplay between spin-orbit coupling, rotation and interatomic interactions can lead to various topological excitations of the BECs [19–26]. Most recently, spin-orbit-coupled spin-1 BECs of ⁸⁷Rb atoms have been realized experimentally [27, 28], which opens another window for the exploration of peculiar physical properties of spin-1 BECs generally inaccessible in pseudo-spin-1/2 BECs and electronic materials due to the competition among the spin-exchange interaction, SOC and the other parameters [29–34].

On the other hand, quantum gases with magnetic dipole-dipole interaction (DDI), especially the BECs with DDI, have also drawn much attention both experimentally [35–38] and theoretically [39–48] in recent years. Relevant studies on spinor BECs with DDI have shown that the interplay between the short-range spin-exchange interaction and the long-range anisotropic DDI can lead to rich topological defects, spin textures and spin dynamics [39, 40]. Therefore it is of particular interest to investigate the combined effects of SOC and DDI on spinor BECs, and this idea has recently attracted extensive attention [14, 32, 49–52]. For instance, an experimental scheme has been proposed by Deng *et al.* to generate SOC in spin-3 Cr atoms using Raman processes [49]. A thermodynamically stable ground state with a meron spin configuration has been predicted in a dipolar pseudo-spin-1/2 BEC with Rashba SOC [50]. In addition, Kato *et al.* studied twisted spin vortices in a spin-1 BEC with Rashba SOC and DDI confined in a cigar-shaped trap [32].

To the best of our knowledge, the existing studies of the BECs with SOC and DDI as mentioned above refer to the nonrotating case. Considering that one of the most striking hallmarks of a superfluid is its response to rotation, in this paper we study the combined effects of rotation, SOC and DDI on the ground-state structure and spin texture of a dipolar spin-1 BEC with SOC confined in a rotating harmonic plus quartic trap (anharmonic trap). Based on such

*Electronic address: linghuawen@ysu.edu.cn

a harmonic plus quartic trap, one can investigate the ground-state and dynamic properties of spin-1 BEC even if the rotation frequency exceeds the trapping frequency. For fixed rotation frequency, a phase diagram is given with respect to the SOC strength and the DDI strength. We find that the system sustains rich ground-state structures including vortex string phase with density peaks (DPs), triangular (square) vortex lattice phase with DPs, checkerboard phase, stripe phase with hidden vortices and antivortices, multi-layer visible vortex necklaces with a hidden giant vortex plus hidden vortex necklaces. For the case of fixed SOC and DDI strengths, with the increase of rotation frequency the system can exhibit pentagonal vortex lattice with DPs, vortex necklaces with DPs and a central Mermin-Ho vortex [53] or with a hidden giant vortex plus hidden vortex necklaces [54, 55]. Furthermore, the system supports exotic spin textures and skyrmion excitations including an antiskyrmion pair, antiskyrmion-antimeron cluster, skyrmion-antiskyrmion lattice, skyrmion-antiskyrmion cluster, skyrmion-antiskyrmion-meron-antimeron lattice, double-layer antimeron necklaces, and composite giant-antiskyrmion-antimeron necklaces.

The paper is organized as follows. The theoretical model for the system is introduced in section 2. In section 3, we present and analyze the topological structures and typical spin textures of the system. Finally we give a brief summary in section 4.

II. THEORETICAL MODEL

By assuming tight confinement in the z -direction, we consider a rotating quasi-two-dimensional (quasi-2D) spin-1 BEC with Rashba SOC and DDI in a harmonic plus quartic trap. In the mean-field approximation, the dynamics of the system obeys the coupled 2D Gross-Pitaevskii (GP) equations [32, 39, 40, 56],

$$i\hbar\frac{\partial\psi_m}{\partial t} = \left(-\frac{\hbar^2}{2M}\nabla^2 + V_{tr} + c_0n - \Omega L_z\right)\psi_m + c_1\sum_{m'=-1}^1\mathbf{F}\cdot\mathbf{f}_{mm'}\psi_{m'} + \sum_{m'=-1}^1(V_{so})_{mm'}\psi_{m'} + c_{dd}\sum_{m'=-1}^1\mathbf{b}\cdot\mathbf{f}_{mm'}\psi_{m'}, \quad (1)$$

where M is the atomic mass, $\psi_m(m = 1, 0, -1)$ is the 2D macroscopic wave function of the atoms condensed in the spin state $|1, m\rangle$, and the total atomic density $n = n_1 + n_0 + n_{-1} = \sum_m|\psi_m|^2$ satisfies $\int n d\mathbf{r} = N$ with N being the total number of atoms. The harmonic plus quartic trap V_{tr} is given by [57]

$$V_{tr} = \frac{1}{2}M\omega_{\perp}^2\left(r_{\perp}^2 + \mu\frac{r_{\perp}^4}{a^2}\right) = \frac{1}{2}\hbar\omega_{\perp}\left(\frac{r_{\perp}^2}{a^2} + \mu\frac{r_{\perp}^4}{a^4}\right), \quad (2)$$

where ω_{\perp} is the radial trap frequency, $r_{\perp} = \sqrt{x^2 + y^2}$, $a = \sqrt{\hbar/M\omega_{\perp}}$, and μ is a dimensionless constant which denotes the anharmonicity of the trap. Ω is the rotation frequency along the z -direction, and $L_z = i\hbar(y\partial_x - x\partial_y)$ is the z component of the angular-momentum operator. The Rashba SOC is expressed by $V_{so} = k(f_x p_x + f_y p_y)$, where k represents the isotropic SOC strength [58, 59], and $p_{\alpha} = -i\hbar\partial_{\alpha}$ ($\alpha = x, y$) is the momentum operator. $c_0 = 4\pi\hbar^2(2a_2 + a_0)\gamma/3M$ and $c_1 = 4\pi\hbar^2(a_2 - a_0)\gamma/3M$ give the strengths of density-density and spin-exchange interactions, respectively. Here $\gamma = \sqrt{M\omega_z/2\pi\hbar}$ with ω_z being the harmonic trap frequency in the z -direction, and a_s ($s = 0, 2$) is the s -wave scattering length for the scattering channel with total spin s . $\mathbf{F} = (F_x, F_y, F_z)$ is the spin vector defined by $F_{\nu}(\mathbf{r}) \equiv \sum_{mm'}\psi_m^*(f_{\nu})_{mm'}\psi_{m'}$ ($\nu = x, y, z$), and $\mathbf{f} = (f_x, f_y, f_z)$ is the vector of 3×3 spin-1 matrices. Concretely, the components of the spin vector \mathbf{F} are expressed as

$$F_x = \frac{1}{\sqrt{2}}[\psi_1^*\psi_0 + \psi_0^*(\psi_1 + \psi_{-1}) + \psi_{-1}^*\psi_0], \quad (3)$$

$$F_y = \frac{i}{\sqrt{2}}[-\psi_1^*\psi_0 + \psi_0^*(\psi_1 - \psi_{-1}) + \psi_{-1}^*\psi_0], \quad (4)$$

$$F_z = |\psi_1|^2 - |\psi_{-1}|^2. \quad (5)$$

The last term on the right-hand side of equation (1) corresponds to the magnetic DDI, where $c_{dd} = \mu_0 g_e^2 \mu_B^2 \gamma / 4\pi$ denotes the DDI coefficient, μ_0 is the vacuum magnetic permeability, μ_B is the Bohr magneton, and g_e is the Landé g -factor. Here \mathbf{b} is the effective 2D dipole field defined by $b_{\nu} \equiv \int d\mathbf{r}'_{\perp} \sum_{\nu\nu'} Q_{\nu\nu'}^{2D} F_{\nu'}$ ($\nu, \nu' = x, y, z$) in which $Q_{\nu\nu'}^{2D}$ is the 2D dipole kernel related to the 3D one. The 3D dipole kernel is given by

$$Q_{\nu\nu'}^{3D}(\mathbf{r} - \mathbf{r}') = \frac{\delta_{\nu\nu'} - 3\hat{r}_{\nu}\hat{r}_{\nu'}}{r^3}, \quad (6)$$

where $\mathbf{r} = (x, y, z)$, $r = |\mathbf{r}|$, $\hat{r} = \mathbf{r}/r$, and $|\mathbf{r} - \mathbf{r}'|$ is the relative position of two dipoles. As the motion of the BEC in the z -direction is frozen in the ground state of harmonic oscillator, we assume a Gaussian profile along the z -direction,

i.e., $\varphi_m(z) = (1/\pi^{1/4}a_z^{1/2})\exp(-z^2/2a_z^2)$ with $a_z = \sqrt{\hbar/M\omega_z}$, then we can reduce $Q_{\nu\nu'}^{3D}$ to $Q_{\nu\nu'}^{2D}$ in two dimensions. The detailed derivation is referred to the relevant literatures [39, 40, 56]. For the sake of numerical calculation, we use the Fourier transform and convolution theorem to express the 2D dipole kernel and the 2D effective dipole field in momentum space, and we obtain

$$\tilde{Q}^{2D}(k_x, k_y) = -\frac{4\pi}{3} \begin{pmatrix} 1 & 0 & 0 \\ 0 & 1 & 0 \\ 0 & 0 & -2 \end{pmatrix} + 4\pi \frac{G\left(\frac{k_\perp a_z}{\sqrt{2}}\right)}{k_\perp^2} \begin{pmatrix} k_x^2 & k_x k_y & 0 \\ k_x k_y & k_y^2 & 0 \\ 0 & 0 & -k_\perp^2 \end{pmatrix}, \quad (7)$$

$$b_\nu = \mathcal{F}^{-1} \left\{ \sum_{\nu'} \tilde{Q}^{2D}(k_x, k_y) \mathcal{F}[F_{\nu'}] \right\}, \quad (8)$$

where $k_\perp = \sqrt{k_x^2 + k_y^2}$, $G(q) \equiv 2qe^{q^2} \int_q^\infty e^{-t^2} dt$, and \mathcal{F} represents the Fourier transform operator [40, 56].

In our calculation, it is convenient to introduce the following notations $\tilde{r}_\perp = r_\perp/a$, $\tilde{t} = \omega_\perp t$, $\tilde{V}_{tr} = V_{tr}/\hbar\omega_\perp = (\tilde{r}^2 + \mu\tilde{r}^4)/2$, $\tilde{\Omega} = \Omega/\omega_\perp$, $\tilde{L}_z = L_z/\hbar$, $\tilde{\psi}_m = \psi_m a/\sqrt{N}$ ($m = 1, 0, -1$), $\tilde{c}_0 = c_0 N/\hbar\omega_\perp a^2$, $\tilde{c}_1 = c_1 N/\hbar\omega_\perp a^2$, $\tilde{k} = k/\omega_\perp a$, and $\tilde{c}_{dd} = c_{dd} N/\hbar\omega_\perp a^2$. Then we obtain the dimensionless coupled GP equations

$$i\frac{\partial\psi_m}{\partial t} = \left(-\frac{1}{2}\nabla^2 + V_{tr} + c_0 n - \Omega L_z \right) \psi_m + c_1 \sum_{m'=-1}^1 \mathbf{F} \cdot \mathbf{f}_{mm'} \psi_{m'} + \sum_{m'=-1}^1 (V_{so})_{mm'} \psi_{m'} + c_{dd} \sum_{m'=-1}^1 \mathbf{b} \cdot \mathbf{f}_{mm'} \psi_{m'}. \quad (9)$$

For simplicity the tilde is omitted throughout this paper.

For spin-1 BEC, the spin texture is defined by [60, 61]

$$S_x = \frac{1}{\sqrt{2}} \frac{\psi_0^* \psi_1 + (\psi_1^* + \psi_{-1}^*) \psi_0 + \psi_0^* \psi_{-1}}{|\psi_1|^2 + |\psi_0|^2 + |\psi_{-1}|^2}, \quad (10)$$

$$S_y = \frac{i}{\sqrt{2}} \frac{\psi_0^* \psi_1 + (\psi_{-1}^* - \psi_1^*) \psi_0 - \psi_0^* \psi_{-1}}{|\psi_1|^2 + |\psi_0|^2 + |\psi_{-1}|^2}, \quad (11)$$

$$S_z = \frac{\psi_1^* \psi_1 - \psi_{-1}^* \psi_{-1}}{|\psi_1|^2 + |\psi_0|^2 + |\psi_{-1}|^2}. \quad (12)$$

The spatial distribution of the topological structure of the system can be well described by the topological charge density

$$q(x, y) = \frac{1}{4\pi} \mathbf{s} \cdot \left(\frac{\partial \mathbf{s}}{\partial x} \times \frac{\partial \mathbf{s}}{\partial y} \right), \quad (13)$$

with $\mathbf{s} = \mathbf{S}/|\mathbf{S}|$, and the topological charge is defined as

$$Q = \int q(x, y) dx dy. \quad (14)$$

The topological charge $|Q|$ is unchanged, no matter how one exchange the components of the spin density vector S_x , S_y and S_z ,

III. RESULTS AND DISCUSSION

Due to the presence of SOC, rotation, nonlocal DDI and nonlinear contact interaction, there is no analytical solution for the coupled nonlinear GP equations (1) and (9). Next, we numerically solve the 2D GP equations (9) to obtain the ground state by minimizing the total energy of the system using the widely adopted imaginary-time propagation method [11, 54, 55]. A remarkable feature of this system is that there are a large number of free parameters, including the rotation frequency, the strength and sign of the density-density interaction and spin-exchange interaction, SOC and DDI, and the anharmonicity of the trap. As a result of the competition among multiple parameters, the system can exhibit rich ground-state structures and unique properties. In order to highlight the effects of the SOC, DDI and rotation, without loss of generality, we fix $\mu = 0.5$, $c_0 = 1000$ and $c_1 = 50$. For other values of μ , c_0 and c_1 , our simulation shows that there exist similar phase diagrams and ground-states configurations.

A. SOC and DDI effects

In this system, rotation effect is dominant compared with SOC and DDI effects. Therefore, in this section we choose a relatively small rotation frequency (for instance, $\Omega = 0.1$ or $\Omega = 0.4$), which can not only reflect the combined effects of SOC, DDI and rotation, but also not highlight the rotation effect. In the case of fixed rotation frequency, we give a ground-state phase diagram spanned by the SOC strength k and the DDI strength c_{dd} . There are five different phases marked by A–E, which differs in terms of their density profiles and phase distributions. In the following discussion, we will give a detailed description of each phase. The density and phase distributions of the five different phases A–E in figure 1 are shown in figures 2(a)–2(e), respectively. In figure 2, the left three columns are the density profiles $|\psi_1|^2$, $|\psi_0|^2$ and $|\psi_{-1}|^2$ of three components $m_F = 1$ (component 1), $m_F = 0$ (component 2) and $m_F = -1$ (component 3), columns 4 to 6 denote the corresponding phase distributions $\theta_1 = \arg \psi_1$, $\theta_0 = \arg \psi_0$ and $\theta_{-1} = \arg \psi_{-1}$, respectively, and the last column represents the total density n .

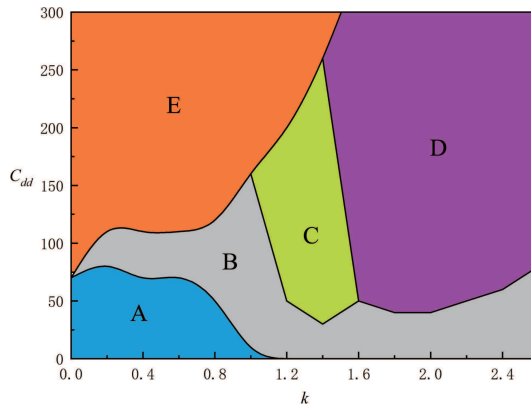


FIG. 1: Ground-state phase diagram of rotating spin-orbit-coupled dipolar spin-1 BEC with respect to k and c_{dd} for $c_0 = 1000$, $c_1 = 50$ and $\Omega = 0.1$. There are five different phases marked by A–E.

We start from the case where the SOC and DDI are weak, which is indicated by the region A in figure 1. In this phase, there exist a hidden vortex [54, 55, 62], a vortex pair or a vortex string in the three components, where the density distribution of $m_F = 1$ component forms two petal-like density peaks which are very similar to two quantum droplets [63, 64], and the phase defects in the components are basically arranged along the same straight line. To distinguish it from other phases, we may call it vortex string phase with DPs. With the increase of SOC or DDI, the A phase transform to the B phase, as shown in figure 1. The density peaks in the three components show evident triangular distribution, with an extra droplet, a vortex or a vortex pair being located in the central region of the trap (see figure 2(b)). At the same time, the vortices except the central ones in the components constitute a triangular vortex lattice. This phase is a typical triangular vortex lattice phase with DPs. In a narrow parameter regime of relatively large SOC strength and DDI strength, the C phase emerges as the ground state. Typical density and phase distributions are given in figure 2(c). The trap center is occupied by a droplet, a vortex and a doubly quantized vortex for the three components, respectively. The main density peaks are arranged in a square. In this context, the C phase is a square vortex lattice phase with DPs. For the case of strong SOC, with the increase of c_{dd} , the B phase transforms to the D phase (checkerboard phase), where the component densities evolve into checkerboard patterns, the vortices in $m_F = 1$ and $m_F = -1$ components disappear, and an alternative vortex-antivortex pair lattice is generated in $m_F = 0$ component (see figure 2(d)). The phenomenon of component separation is significantly enhanced in the checkerboard phase.

In the limit of strong DDI but weak SOC, the system sustains E phase. Typical density and phase distributions of such a phase are shown in figure 2(e), where stripe density patterns are created in individual components, and there are only few hidden vortices plus hidden antivortices, and some ghost vortices [54, 65] as well as ghost antivortices distributed in outskirts of the atom cloud. Thus the E phase is a stripe phase. In addition, for the A–C phases, the total densities show typical Thomas-Fermi (TF) distribution. By contrast, for the D phase and the E phase, the total densities exhibit checkerboard pattern and stripe pattern, respectively. Note that here the stripe phase (E phase) is remarkably different from the irregular stripe phase reported in a spin-orbit-coupled dipolar spin-1 BEC without spin-exchange interaction in a cigar-shaped 3D harmonic trap [32]. The latter case exists for strong SOC but with weak DDI, where each component density shows no symmetry with respect to the two principal axes of the atom cloud, the total density exhibits TF distribution, and the spin texture has a spin stripe structure (see figure 2(a) in Ref. [32]). However, in the present system, the stripe state exists for strong DDI but with weak or relatively weak

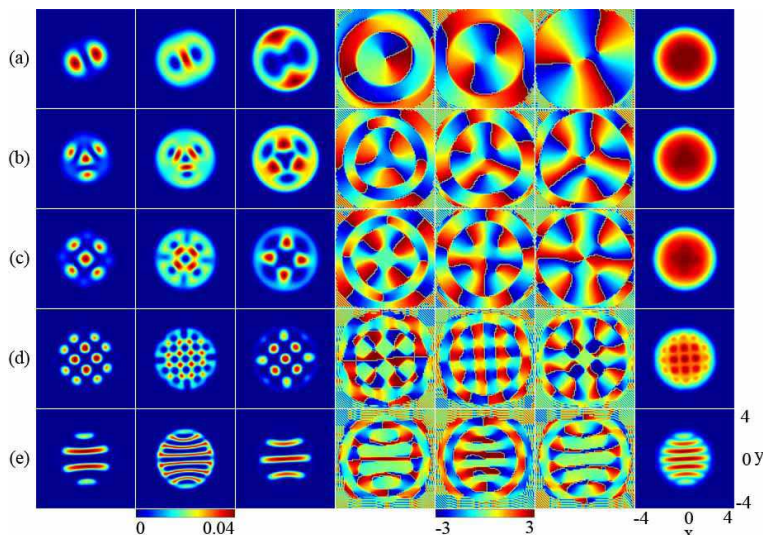


FIG. 2: Typical ground states of spin-1 BECs with SOC and DDI in a rotating harmonic plus quartic trap, where $\Omega = 0.1$. Rows (a)–(e) correspond to the A–E phases in figure 1, respectively. (a) $k = 0.8$, $c_{dd} = 40$, (b) $k = 1.4$, $c_{dd} = 20$, (c) $k = 1.4$, $c_{dd} = 50$, (d) $k = 2$, $c_{dd} = 300$, and (e) $k = 0.8$, $c_{dd} = 300$. The columns from left to right denote $|\psi_1|^2$, $|\psi_0|^2$, $|\psi_{-1}|^2$, $\arg\psi_1$, $\arg\psi_0$, $\arg\psi_{-1}$, and the total density $n = \sum_m |\psi_m|^2$ ($m = 1, 0, -1$), respectively. The unit length is a .

SOC, where both the component densities and the total density exhibit good symmetry concerning the principal axes of the atom cloud, and the spin texture is an exotic skyrmion-antiskyrmion-half-skyrmion-half-antiskyrmion lattice (see figure 6(d)). This point is due to the complex competition between SOC, DDI, rotation, spin-exchange interaction and density-density interaction.

To analyze and compare the effects of SOC and DDI on the ground-state of the system, in figure 3 we show the density and phase distributions of spin-1 BECs with various SOC strengths or DDI strengths in a rotating anharmonic trap. For weak SOC ($k = 0.8$), the system shows a triangular vortex lattice structure with isolated DPs (see figure 3(a)), where for component 1 there is a vortex at the trap center surrounded by several ghost vortices, a visible triangular vortex lattice and a central antivortex are generated in component 2 with several ghost vortices and antivortices being distributed in the outskirts of the cloud, and a hidden triangular vortex lattice is formed in component 3. When k increases to 1.2 (figure 3(b)), there are four obvious DPs in component 1 with a doubly quantized vortex at the trap center, and a square vortex lattice is formed in component 3. At the same time, a square vortex lattice and a central antivortex constitute a visible criss-cross vortex string lattice in component 2. Thus we may call it square vortex lattice with DPs. With the further increase of k , e.g., $k = 2.4$, the ground state of the system becomes a checkerboard phase (figure 3(c)), which is similar to that in Fig. 2(e). From figures 3(a)-3(c), it is shown that the increase of SOC strength can lead to a structural phase transition from a triangular vortex lattice with DPs to a square vortex lattice with DPs and then to a checkerboard phase. Physically, this phenomenon is induced by the spin-orbit interaction between the atomic spin and the center-of-mass motion of the BEC. Therefore varying the SOC strength will result in the change of the atomic spin structure and the spin texture of the system. When the SOC strength increases, the DP number and the vortex (or antivortex) number in each component evidently increases because the stronger SOC means there is a larger orbital angular momentum and more energy input into the system [8, 19]. On the other hand, the interplay among SOC, DDI, rotation and contact interaction will change the symmetry of vortex distribution in the system. Consequently, for strong SOC, the checkerboard phase rather than a triangular vortex lattice phase, dominates the topological structure of the system.

Figures 3(d)-3(f) illustrate the effect of DDI on the ground-state structure of the system, where $k = 1.8$ and $\Omega = 0.4$. For weak DDI, e.g., $c_{dd} = 1$, the ground state displays obvious vortex chain structure in which three vortex chains in each component form an angle of $2\pi/3$ degrees with each other as shown in figure 3(d). When the DDI strength increases to $c_{dd} = 300$, the checkerboard phase becomes the ground-state phase of the system (see figure 3(e)). For the larger DDI strength $c_{dd} = 800$, the checkerboard phase transforms into a tripe phase as displayed in figure 3(f). Different from figures 2(d)-2(e) and 3(a)-3(c), the structural phase transition from figure 3(d) to figure 3(f) and then to figure 3(e) is mainly dominated by DDI.

The z component of the orbital angular momentum, $\langle L_z \rangle = \int \psi^\dagger(\mathbf{r})(xp_y - yp_x)\psi(\mathbf{r})d\mathbf{r}$ with $\psi(\mathbf{r}) = (\psi_1, \psi_0, \psi_{-1})^T$, is important in considering this system. Figure 4 displays $\langle L_z \rangle$ as a function of k for $c_{dd} = 100$ and $\Omega = 0.1$, where B–E correspond to the B–E phases in figure 1, respectively. The E phase (i.e., the stripe phase) scarcely has

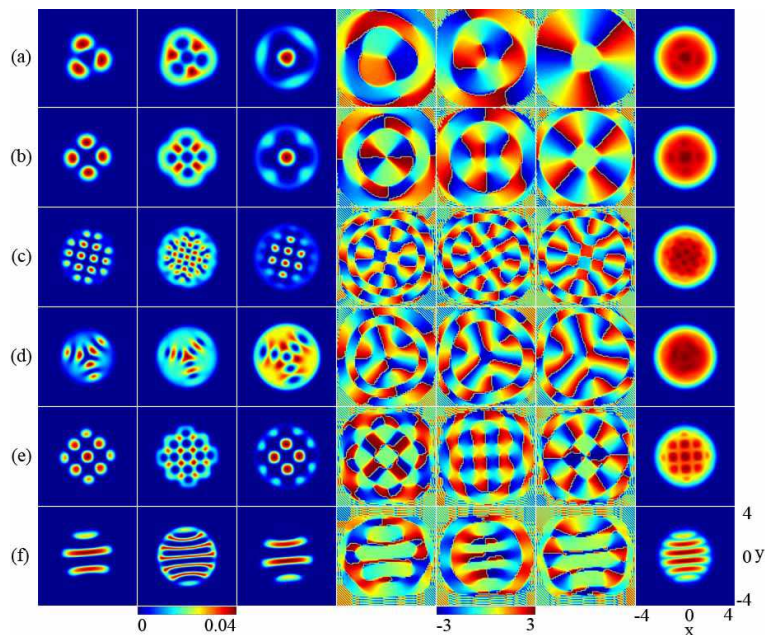


FIG. 3: Ground-state density distributions and phase distributions of spin-1 BECs with SOC and DDI in a rotating harmonic plus quartic trap. The top three rows: $c_{dd} = 100$, $\Omega = 0.1$, (a) $k = 0.8$, (b) $k = 1.2$, and (c) $k = 2.4$. The bottom three rows: $k = 1.8$, $\Omega = 0.4$, (d) $c_{dd} = 1$, (e) $c_{dd} = 300$, and (f) $c_{dd} = 800$. The other parameters are the same with those in figures 1 and 2. The columns from left to right denote $|\psi_1|^2$, $|\psi_0|^2$, $|\psi_{-1}|^2$, $\arg\psi_1$, $\arg\psi_0$, $\arg\psi_{-1}$, and the total density n , respectively. The unit length is a .

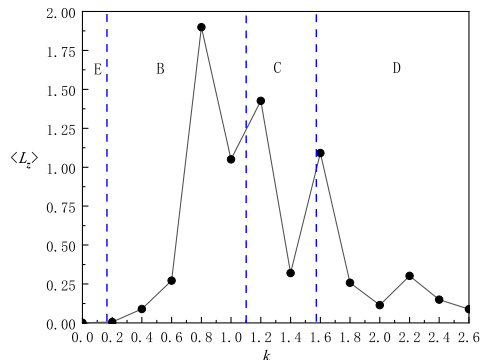


FIG. 4: Orbital angular momentum $\langle L_z \rangle$ as a function of k for $c_{dd} = 100$ and $\Omega = 0.1$. The vertical dotted lines separate the phases and the solid curve demonstrates the trend.

angular momentum because there are only few hidden vortices and antivortices, and ghost vortices plus antivortices. Especially, the ghost vortices (or antivortices) neither carry angular momentum nor energy. The first rapid increase in $\langle L_z \rangle$ occurs in the B phase ($0.18 \lesssim k \lesssim 0.8$) due to there being typical triangular vortex lattice, $\langle L_z \rangle$ reaches the maximum at $k \simeq 0.8$ and then decreases significantly at $k \simeq 1.0$. With an increase of SOC strength, the ground state transforms to the C phase and the angular momentum increases suddenly. The change trend of $\langle L_z \rangle$ in the C phase is similar to that in the B phase. Although $\langle L_z \rangle$ fluctuates in the D phase, which is similar to the B and C phases, on average, the angular momentum is obviously decreasing. The main reason is that for the checkerboard phase there is a vortex-antivortex pair lattice in the $m_F = 0$ component and there are no vortices in the $m_F = 1$ and $m_F = -1$ components. From figure 4, the curve of $\langle L_z \rangle$ and k shows no linear correlation due to the complicated competition among the anisotropic DDI, SOC, rotation, and nonlinear contact interaction.

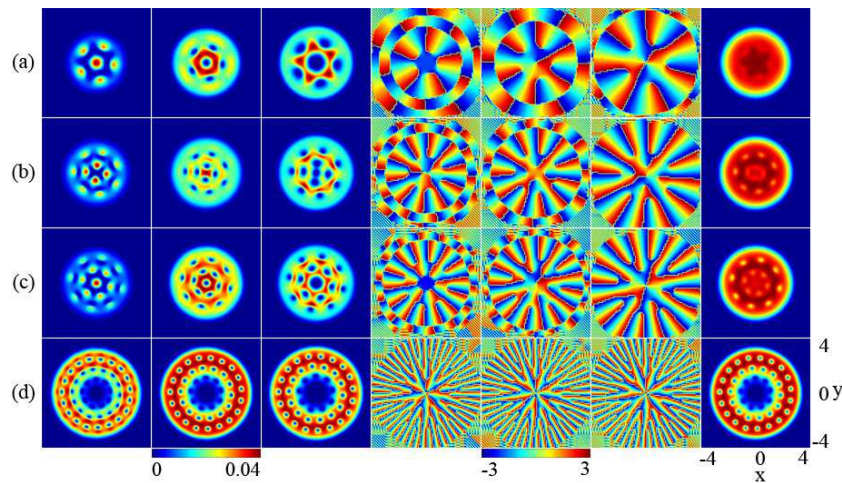


FIG. 5: Ground states of spin-1 BECs with SOC and DDI in a rotating harmonic plus quartic trap, where $c_0 = 1000$, $c_1 = 50$, $k = 1.4$, and $c_{dd} = 50$. (a) $\Omega = 0.4$, (b) $\Omega = 1.2$, (c) $\Omega = 1.4$, and (d) $\Omega = 3$. The columns from left to right denote $|\psi_1|^2$, $|\psi_0|^2$, $|\psi_{-1}|^2$, $\arg\psi_1$, $\arg\psi_0$, $\arg\psi_{-1}$ and the total density n , respectively. The unit length is a .

B. Rotation effect

Next, we consider the influence of rotation on the ground state of the system with given DDI strength and SOC strength. In figure 5, we show the density distributions, the phase distributions and the total densities for the ground states of spin-1 BECs with DDI and SOC in a rotating anharmonic trap. Here $k = 1.4$, $c_{dd} = 50$, and rotation frequencies in rows (a)–(d) are $\Omega = 0.4$, 1.2 , 1.4 , and 3.0 , respectively. For relatively small rotation frequency $\Omega = 0.4$, the density and phase profiles of three components exhibit obvious differences (see figure 5(a)). The $m_F = 1$ component forms a petal-like structure with a central density droplet, and there is a hidden pentagonal vortex lattice. By comparison, a visible pentagonal vortex lattice exists in $m_F = 0$ and $m_F = -1$ components, and there is an additional central density hole for $m_F = 0$ component and $m_F = -1$ component, respectively. The two central density holes in $m_F = 0$ and $m_F = -1$ components correspond to a singly quantized vortex encircled by pentagonal density peaks and a doubly quantized vortex surrounded by pentagram density peaks, respectively.

When the rotation frequency increases to $\Omega = 1.2$, more density petals are generated along the azimuthal direction in the $m_F = 1$ component, and the non-central vortices in each component are distributed along a circle, as shown in figure 5(b). At the same time, the central regions of individual components are occupied by a triangular vortex lattice, a density peak, and criss-cross vortex trains, respectively. Our numerical results show that with the increase of rotation frequency not only the number of vortices along a single circle but also the number of circles increases, as displayed in figures 5(b) and 5(c). In particular, for large rotation frequency, e.g., $\Omega = 3$, the system exhibits an interesting and unique ground-state structure as shown in figure 5(d). There is an almost full overlap of the density profiles and the phase profiles of the three components. Here the visible vortices form multi-layer ringlike structures, i.e., multi-layer visible vortex necklaces. Our numerical simulation shows that the region of the large density hole in each component is occupied by several hidden vortex necklaces and a central hidden giant vortex (see figure 5(d)), which is quite different from the common prediction results in rotating spin-orbit-coupled BECs in a harmonic trap [19–22, 25]. For the latter case, the large density hole in the density profile at large rotation frequency characterizes a pure giant vortex. In addition, the phase mixing of the three components can be understood. Physically, the rapid rotation or the strong SOC will lead to large kinetic energy. Here, the kinetic energy acts against the interspecies contact interaction and DDI. The latter is responsible to component separation while the former tends to expand the BECs and therefore sustains component mixing. At the same time, the anharmonic external potential tends to trap the BECs more tightly and hence also favors component mixing. Consequently, component demixing can be suppressed by the kinetic energy and external trapping potential in some conditions as shown in figure 5(d). Essentially, the topological states of the system in figures 5(a)–5(c) are coreless vortex states because there are no singular points in the total density of the system while that in figure 5(d) corresponds to a nucleated vortex state as there are obvious singular points in the total density, which indicates the increase in rotation frequency can lead to a series of structural phase transitions. Furthermore, we can conclude that for the case of large Ω the rotation effect plays a key role in determining the ground-state phase of the system compared with the DDI effect and the SOC effect.

Based on the above discussion, as three new degrees of freedom, SOC, DDI and rotation frequency can be used to achieve the desired ground-state phases and to control the phase transitions between various ground states of spin-1

BECs in a harmonic plus quartic trap.

C. Topological charge densities and spin textures

To further elucidate the ground-state properties, we now analyze the topological charge densities and spin texture of the system. In figure 6, we show the topological charge densities (column 1) and the spin textures (column 2) of the system in the left two columns, and the local amplifications of the spin textures are displayed in the right two columns. The ground states for figures 6(a)-6(d) are given in figures 2(a), 2(b), 2(d), and 2(e), respectively. Shown in figure 7 are the topological charge densities, the spin textures, and the local enlargements of the spin textures for the parameters in figures 3(a), 3(c), 5(b), and 5(c). For the sake of discussion, we use red square (or rectangle), red circle, blue triangle, blue hexagon, and blue diamond to denote a skyrmion [66], a half-skyrmion (meron) [53], an antiskyrmion, a half-antiskyrmion (antimeron), and a giant antiskyrmion, respectively.

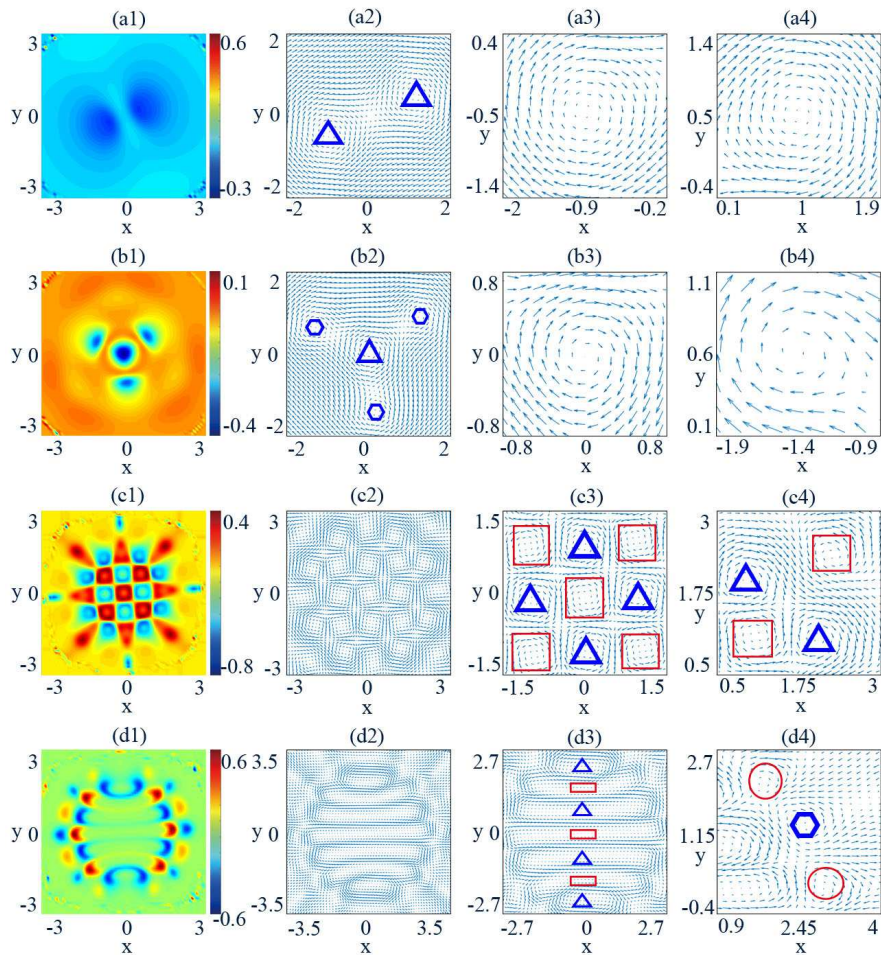


FIG. 6: Topological charge densities and spin textures of rotating spin-1 BECs with DDI and SOC in a harmonic plus quartic trap, where the corresponding ground states for (a)-(d) are given in figures 2(a), 2(b), 2(d), and 2(e), respectively. The first column (from left to right) represents topological charge density, the second column is spin texture, and the right two columns denote the local amplifications of the spin texture. The red square (or rectangle), red circle, blue triangle, and blue hexagon denote a skyrmion, a half-skyrmion, an antiskyrmion, and a half-antiskyrmion, respectively. The unit length is a .

Our computation results show that the local topological charges in figures 6(a3) and 6(a4) approach $Q = -1$, which indicates that the local topological defects in figures 6(a3) and 6(a4) are circular antiskyrmions. Thus the spin texture in figure 6(a2) forms a fascinating antiskyrmion pair. The spin defect in figure 6(b2) is an antiskyrmion-half-antiskyrmion (antiskyrmion-antimeron) cluster [25, 53, 61, 66], where the two local enlargements in figures 6(b3) and 6(b4) correspond to an antiskyrmion and a half-antiskyrmion (antimeron), respectively. In particular, the topological charge density in figure 6(c1) shows a checkerboard pattern, and the spin texture is displayed in figure 6(c2), where

the local amplifications of the spin texture are exhibited in figures 6(c3) and 6(c4). It is shown that the topological structure in figure 6(c2) is an interesting interlaced skyrmion-antiskyrmion lattice consists of skyrmions with unit topological charge $Q = 1$ and antiskyrmions with topological charge $Q = -1$. From figure 6(d3), we can see that there is a staggered skyrmion-antiskyrmion chain along the y direction. At the same time, the local topological defects in figure 6(d4) are three interlaced half-skyrmions (merons) and half-antiskyrmion (antimeron). Thus the topological structure in figure 6(d2) is an exotic complex skyrmion-antiskyrmion-meron-antimeron lattice composed of a staggered skyrmion-antiskyrmion chain and an outer circular interlaced meron-antimeron string.

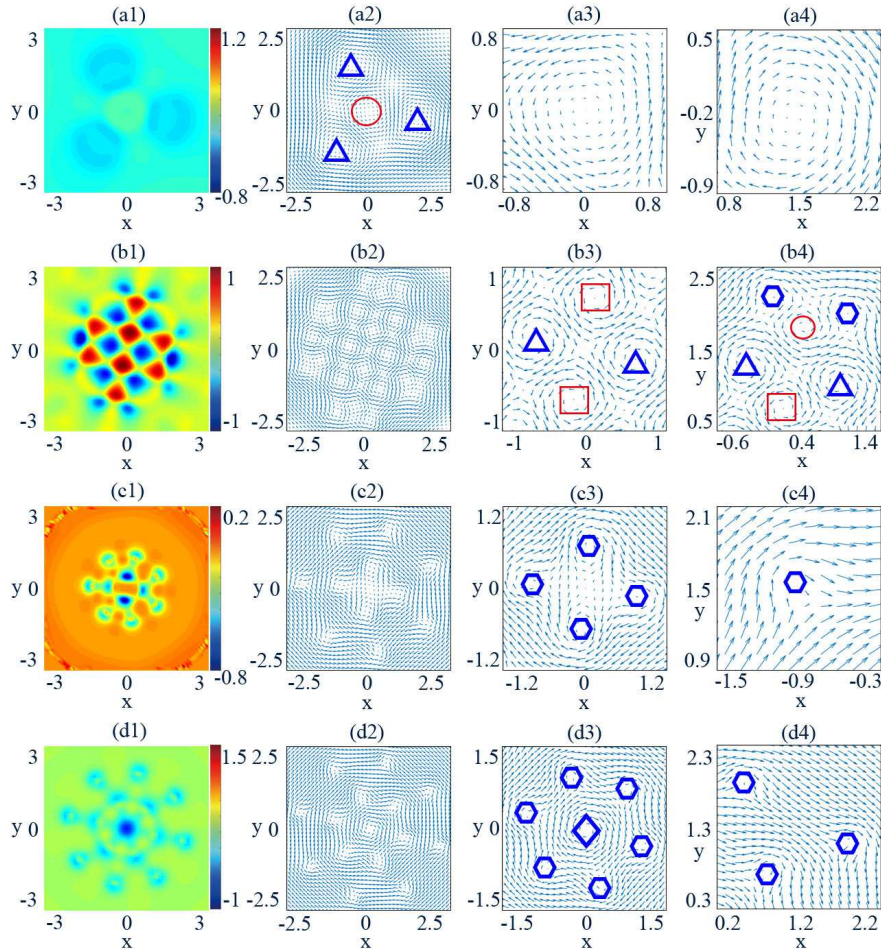


FIG. 7: Topological charge densities and spin textures of rotating spin-1 BECs with DDI and SOC in a harmonic plus quartic trap, where the corresponding ground states for (a)-(d) are given in figures 3(a), 3(c), 5(b), and 5(c), respectively. The first column represents topological charge density, the second column is spin texture, and the right two columns denote the local amplifications of the spin texture. The red square, red circle, blue triangle, blue hexagon, and blue diamond represent a skyrmion, a half-skyrmion, an antiskyrmion, a half-antiskyrmion, and a giant antiskyrmion, respectively. The unit length is a .

Finally, the topological charge densities and spin textures in figure 7 are richer and more interesting, where the ground states are displayed in figures 3(a), 3(c), 5(b), and 5(c). Our numerical calculation shows that the local topological charges in figures 7(a3) and 7(a4) are $Q = 1$ and $Q = -1$, respectively. Therefore the spin texture in figure 7(a2) is a special skyrmion-antiskyrmion cluster composed of a central skyrmion and an outer triangular antiskyrmion lattice. The topological charge density in figure 7(b1) exhibits an obvious checkerboard pattern, which is somewhat similar to that in figure 6(c1). However, our simulation demonstrates that the topological structure in figure 7(b2) is quite different from that in figure 6(c2). As a matter of fact, the local topological defects in figure 7(b3) are alternating skyrmions and antiskyrmions, and the those in figure 7(b4) include a skyrmion, two antiskyrmions, a half-skyrmion (meron) with topological charge $Q = 0.5$, and two half-antiskyrmions (antimerons) with respective topological charge $Q = -0.5$, which indicates the spin defects in figure 7(b2) constitute a rather complicated skyrmion-antiskyrmion-meron-antimeron lattice. From figures 7(c2)-7(c4), one can see that the topological structure in figure 7(c2) is peculiar double-layer and concentric half-antiskyrmion necklaces. Particularly, the topological charge density

in figure 7(d1) has excellent discrete rotational symmetry, which implies that a new type of peculiar topological excitation is generated in the system. Our simulation verifies that the spin defect in the central region of the trap potential is a giant antiskyrmion with local topological charge $Q = -2$, and the other six spin defects are six half-antiskyrmions (antimerons) with respective topological charge $Q = -0.5$ constituting a half-antiskyrmion (antimeron) necklace, as shown in figure 7(d3). From figures 7(d2)-7(d4), we can conclude that the topological structure in figure 7(d2) is composite giant-antiskyrmion-antimeron necklaces made of a central giant antiskyrmion and two concentric antimeron necklaces.

To the best of our knowledge, these new skyrmion excitations observed in the present system are remarkably different from previously reported skyrmion structures in other physical systems, such as rotating two-component BECs with or without SOC (DDI) [8, 10, 19, 21–24, 26, 67, 68], rotating and rapidly quenched spin-1 BECs with SOC in a harmonic trap [31], and non-rotating spin-1 BECs with SOC and DDI in a cigar-shaped trap [32]. In addition, these novel topological excitations (including vortex excitations and skyrmion excitations) in the present work allows to be tested and verified in future experiments.

IV. CONCLUSION

In summary, we have investigated a rich variety of ground-state phases and topological defects of rotating spin-1 BECs with SOC and DDI in a harmonic plus quartic trap. The combined effects of SOC, DDI and rotation on the ground-state configurations and spin textures of the system are analyzed systematically. For fixed rotation frequency, a ground-state phase diagram is given with respect to SOC strength and DDI strength. The system can show rich ground-state phases including vortex string phase with DPs, triangular (square, pentagonal) vortex lattice phase with DPs, checkerboard phase, stripe phase with hidden vortices and antivortices, multi-layer vortex necklaces with a giant vortex and hidden vortex necklaces, depending on the complex competition between the SOC, DDI and rotation. The increase of SOC strength or DDI strength or rotation frequency can lead to a series of structural phase transitions, such as the transition from a square vortex lattice phase with DPs to a checkerboard phase, the switching from a checkerboard phase to a stripe phase, and the transition from a pentagonal vortex lattice phase with DPs to multi-layer vortex necklaces. In addition, the system favors exotic new skyrmion excitations, such as an antiskyrmion pair, antiskyrmion-antimeron cluster, skyrmion-antiskyrmion lattice, skyrmion-antiskyrmion cluster, skyrmion-antiskyrmion-meron-antimeron lattice, double-layer half-antiskyrmion necklaces, and composite giant-antiskyrmion-antimeron necklaces. It is shown that for small rotation frequency, the SOC effect and DDI effect play a key role in determining the ground phase of the system, while for large rotation frequency, the rotation effect is dominant. Furthermore, as three important degrees of freedom, the DDI, SOC, and rotation can be used to achieve the desired ground-state phases and to control the phase transition between various ground states of spin-1 BECs in an anharmonic trap. As the ground states are stable against perturbation and have longer lifetime in contrast to the other stationary states of the system, we expect that the ground-state structures and topological defects of the system can be tested and observed in the future cold atom experiments. The findings in the present work have enriched our new understanding for topological excitations in cold atom physics and condensed matter physics.

Acknowledgments

This work was partially carried out during a visit of the corresponding author (LW) to the research group of Professor W. Vincent Liu at The University of Pittsburgh. The authors are extremely grateful to anonymous reviewers for their careful reading of the manuscript, insightful comments and constructive suggestions. This work was supported by the National Natural Science Foundation of China (Grant Nos. 11475144 and 11047033), the Natural Science Foundation of Hebei Province (Grant Nos. A2019203049 and A2015203037), and Research Foundation of Yanshan University (Grant No. B846).

-
- [1] Zutic I, Fabian J and Das Sarma S 2004 *Rev. Mod. Phys.* **76** 323
 - [2] Qi X L and Zhang S C 2011 *Rev. Mod. Phys.* **83** 1057
 - [3] Lin Y J, Jiménez-García K and Spielman I B 2011 *Nature* **471** 83
 - [4] Wang P, Yu Z Q, Fu Z, Miao J, Huang L, Chai S, Zhai H and Zhang J 2012 *Phys. Rev. Lett.* **109** 095301
 - [5] Wu Z, Zhang L, Sun W, Xu X T, Wang B Z, Ji S C, Deng Y, Chen S, Liu X J and Pan J W 2016 *Science* **354** 83
 - [6] Huang L, Meng Z, Wang P, Peng P, S Zhang, Chen L, Li D, Zhou Q and Zhang J 2016 *Nat. Phys.* **12** 540
 - [7] Li J R, Lee J, Huang W, Burchesky S, Shteynas B, Top F C, Jamison A O and Ketterle W 2017 *Nature* **543** 91

- [8] Zhai H 2015 *Rep. Prog. Phys.* **78** 026001
- [9] Sinha S, Nath R and Santos L 2011 *Phys. Rev. Lett.* **107** 270401
- [10] Hu H, Ramachandhran B, Pu H and Liu X J 2012 *Phys. Rev. Lett.* **108** 010402
- [11] Zhang Y, Mao L and Zhang C 2012 *Phys. Rev. Lett.* **108** 035302
- [12] Kawakami T, Mizushima T, Nitta M and Machida K 2012 *Phys. Rev. Lett.* **109** 015301
- [13] Qu C, Hamner C, Gong M, Zhang C and Engels P 2013 *Phys. Rev. A* **88** 021604(R)
- [14] Xu Y, Zhang Y and Wu B 2013 *Phys. Rev. A* **87** 013614
- [15] Stringari S 2017 *Phys. Rev. Lett.* **118** 145302
- [16] Kartashov Y V and Konotop V V 2017 *Phys. Rev. Lett.* **118** 190401
- [17] Li X, Wang Q, Wang H, Shi C, Jardine M and Wen L 2019 *J. Phys. B* **52** 155302
- [18] Fan Z, Chen Z, Li Y and Malomed B A 2020 *Phys. Rev. A* **101** 013607
- [19] Xu X Q and Han J H 2011 *Phys. Rev. Lett.* **107** 200401
- [20] Radic J, Sedrakyan T A, Spielman I B and Galitski V 2011 *Phys. Rev. A* **84** 063604
- [21] Zhou X, Zhou J and Wu C 2011 *Phys. Rev. A* **84** 063624
- [22] Aftalion A and Mason P 2013 *Phys. Rev. A* **88** 023610
- [23] Wang H, Wen L, Yang H, Shi C and Li J 2017 *J. Phys. B* **50** 155301
- [24] Zhang X F, Kato M, Han W, Zhang S G, Saito H 2017 *Phys. Rev. A* **95** 033620
- [25] Liu C F, Fan H, Zhang Y C, Wang D S and Liu W M 2012 *Phys. Rev. A* **86** 053616
- [26] Yang H, Wang Q, Su N and Wen L 2019 *Eur. Phys. J. Plus* **134** 589
- [27] Campbell D L, Price R M, Putra A, Valdes-Curiel A, Trypogeorgos D and Spielman I B 2016 *Nat. Commun.* **7** 10897
- [28] Luo X, Wu L, Chen J, Guan Q, Gao K, Xu Z F, You L and Wang R 2016 *Sci. Rep.* **6** 18983
- [29] Wang C, Gao C, Jian C M and Zhai H 2010 *Phys. Rev. Lett.* **105** 160403
- [30] Ruokokoski E, Huhtamäki J A M and Möttönen M 2012 *Phys. Rev. A* **86** 051607
- [31] Liu C F and Liu W M 2012 *Phys. Rev. A* **86** 033602
- [32] Kato M, Zhang X F, Sasaki D and Saito H 2016 *Phys. Rev. A* **94** 043633
- [33] Chen L, Zhu C, Zhang Y and Pu H 2018 *Phys. Rev. A* **97** 031601(R)
- [34] Adhikari S K 2019 *Phys. Rev. A* **100** 063618
- [35] Griesmaier A, Werner J, Hensler S, Stuhler J and Pfau T 2005 *Phys. Rev. Lett.* **94** 160401
- [36] Ray M W, Ruokokoski E, Tiurev K, Möttönen M and Hall D S 2015 *Science* **348** 544
- [37] Chomaz L, van Bijnen R M W, Petter D, Faraoni G, Baier S, Becher J H, Mark M J, Wächtler F, Santos L and Ferlaino F 2018 *Nat. Phys.* **14** 442
- [38] Tanzi L, Lucioni E, Famà F, Catani J, Fioretti A, Gabbanini C, Bisset R N, Santos L and Modugno G 2019 *Phys. Rev. Lett.* **122** 130405
- [39] Lahaye T, Menotti C, Santos L, Lewenstein M and Pfau T 2009 *Rep. Prog. Phys.* **72** 126401
- [40] Kawaguchi Y and Ueda M 2012 *Phys. Rep.* **5** 520
- [41] Goral K, Rzazewski K and Pfau T 2000 *Phys. Rev. A* **61** 051601
- [42] Yi S and You L 2000 *Phys. Rev. A* **61** 041604
- [43] Santos L, Shlyapnikov G V and Lewenstein M 2003 *Phys. Rev. Lett.* **90** 250403
- [44] Malet F, Kristensen T, Reimann S M and Kavoulakis G M 2011 *Phys. Rev. A* **83** 033628
- [45] Liu B, Li X, Yin L and Liu W V 2015 *Phys. Rev. Lett.* **114** 04530
- [46] Chä S-Y and Fischer U R 2017 *Phys. Rev. Lett.* **118** 130404
- [47] Borgh M O, Lovegrove J and Ruostekoski J 2017 *Phys. Rev. A* **95** 053601
- [48] Bisset R N, Blakie P B and Stringari S 2019 *Phys. Rev. A* **100** 013620
- [49] Deng Y, Cheng J, Jing H, Sun C P and Yi S 2012 *Phys. Rev. Lett.* **108** 125301
- [50] Wilson R M, Anderson B M and Clark C W 2013 *Phys. Rev. Lett.* **111** 185303
- [51] Gopalakrishnan S, Martin I and Demler E A 2013 *Phys. Rev. Lett.* **111** 185304
- [52] Huang C, Ye Y, Liu S, He H, Pang W, Malomed B A and Li Y 2018 *Phys. Rev. A* **97** 013636
- [53] Mermin N D and Ho T L 1976 *Phys. Rev. Lett.* **36** 594
- [54] Wen L, Xiong H and Wu B 2010 *Phys. Rev. A* **82** 053627
- [55] Wen L and Li J 2014 *Phys. Rev. A* **90** 053621
- [56] Kawaguchi Y, Saito H, Kudo K and Ueda M 2010 *Phys. Rev. A* **82** 043627
- [57] Fetter A L, Jackson B and Stringari S 2005 *Phys. Rev. A* **71** 013605
- [58] Xu Z-F, Kobayashi S and Ueda M 2013 *Phys. Rev. A* **88** 013621
- [59] Li J, Yu Y-M, Zhuang L and Liu W-M 2017 *Phys. Rev. A* **95** 043633
- [60] Mizushima T, Kobayashi N and Machida K 2004 *Phys. Rev. A* **70** 043613
- [61] Kasamatsu K, Tsubota M and Ueda M 2005 *Phys. Rev. A* **71** 043611
- [62] Wen L, Qiao Y, Xu Y and Mao L 2013 *Phys. Rev. A* **87** 033604
- [63] Ferrier-Barbut I, Kadau H, Schmitt M, Wenzel M and Pfau T 2016 *Phys. Rev. Lett.* **116** 215301
- [64] Kartashov Y V, Malomed B A and Torner L 2019 *Phys. Rev. Lett.* **122** 193902
- [65] Tsubota M, Kasamatsu K and Ueda M 2002 *Phys. Rev. A* **65** 023603
- [66] Skyrme T H R 1962 *Nucl. Phys.* **31** 556
- [67] Zhang X F, Han W, Jiang H F, Liu W M, Saito H and Zhang S G 2016 *Ann. Phys.* **375** 368
- [68] Fetter A L 2009 *Rev. Mod. Phys.* **81** 647